

Emergence of human oculomotor behavior in a cable-driven biomimetic robotic eye using optimal control

Reza Javanmard Alitappeh^{*,†}, Akhil John[†], Bernardo Dias[†], A. John van Opstal⁺,
and Alexandre Bernardino[†], *Senior Member, IEEE*

Abstract—This paper explores the application of model-based optimal control principles in understanding stereotyped human oculomotor behaviors. Using a realistic model of the human eye with a six-muscle cable-driven actuation system, we tackle the novel challenges of addressing a system with six degrees of freedom. We apply nonlinear optimal control techniques to optimize accuracy, energy, and duration of eye movement trajectories. Employing a recurrent neural network to emulate system dynamics, we focus on generating rapid, unconstrained saccadic eye movements. Remarkably, our model replicates realistic three-dimensional rotational kinematics and dynamics observed in human saccades, with the six cables organizing themselves into appropriate antagonistic muscle pairs, resembling the primate oculomotor system.

Index Terms—Oculomotor system; Saccadic Eye Movements; Biologically Inspired Robots; Recurrent neural network; Listing's law; Optimization and Optimal Control; Cable-Driven Robot; Cable pre-tension.

I. INTRODUCTION

With the increasing use of robots in our daily lives, **birobotics**¹ is becoming an important topic for researchers in the fields of robotics and biology. Both robots and humans have sensors to perceive the environment and actuators to perform actions. Therefore, designing a control system that allows robots to behave as humans or animals is an important goal in this multidisciplinary research field. In this sense, robots can be designed to mimic the natural behavior of humans and animals, and biologists can use the results from the artificial models without having to face the ethical and technical difficulties of experiments on the real model. This interdisciplinary work helps roboticists develop better robot designs and control systems [1], but robotics can also be used to explain the emergence of biological behavior [2]. Several such attempts have been published, e.g., on robotic models of cockroaches and hexapedal robots [3], [4], and of insects (such as ants and bees) [5], [4]. Biomimetic robotics has also been applied to biologically equivalent body parts, such as, e.g., the hand [6], and the eye [7], [8]. Robot models have also

been used to study gaze behaviors of humans. Gaze plays an important role in social interactions, signaling one's attention to external events, but also to attitudes, affects, or emotions [9].

Optimal control is a paradigm frequently used in the study of neuro-musculoskeletal systems [10]. However, most of the research focuses on the human biomechanics of the limbs and spine [11]. Only a few studies have proposed the use of optimal control theory in modeling human eye movements [12], [13], [14], [15] but no one has considered the full complexity of the 3D motion controlled by the six extraocular muscles. In this paper, we propose a novel unconstrained biomimetic robotic eye model to study the emergence of the characteristics of human saccadic eye movements. Compared to other works, our contributions in this paper are as follows:

- We designed a 6 DoF cable-driven robot with realistic cable insertions and unconstrained movements.
- We used the model to analyze both the kinematic and dynamic properties of saccades in 3D.
- The full dynamics of the robotic eye was extracted by training a non-linear recursive neural network (NARX).
- We show the emergence of human-like saccades using optimal control to drive the nonlinear robotic eye model.

The paper is organized as follows. Section II describes the kinematic and dynamic properties of saccades found in physiology that reflect a tightly coordinated synergy of the extraocular muscles, for which the neuronal control mechanisms are still largely unknown. In Section III we review other existing robot eye models and show that all lack important mechanical properties to study the emergence of human-like saccades with similar characteristics as found in physiology. In particular, so far no studies have presented a model with full 3D unconstrained saccadic movements actuated by 6 muscle-like actuators. In Section IV we present our formulation for biomimetic saccade control in robot eyes, following an optimal control approach applied to a suitable simulator of the eye model. In Section V we describe the mechanical design of our biomimetic eye and its novel characteristics that allow for a study of oculomotor control that is more complete than in other existing models. Sections VI and VII specify the methods used to model and control our system. The results of the simulations are presented in Section VIII, where we show that the proposed approach exhibits properties similar to those found in biology. These properties are not preprogrammed in the system, but

[†]Institute for Systems and Robotics, Instituto Superior Técnico, ISR, Lisbon, Portugal, ⁺Section Neurophysics, Donders Centre for Neuroscience, Radboud University, Nijmegen, The Netherlands, *University of Science and Technology of Mazandaran, Behshahr, Iran.

Corresponding author: Reza Javanmard Alitappeh (email: Rezajavanmard64@gmail.com).

¹robots inspired by human or animal biological behavior

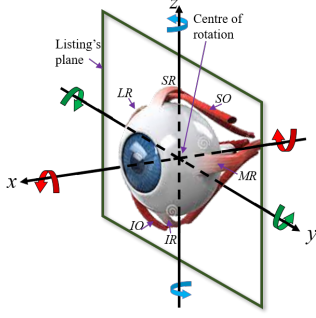


Fig. 1. Representation of the right human eye with its six extraocular muscles. The muscles can rotate the eye in any three-dimensional orientation around its fixed center of rotation. The right-handed head-fixed reference frame of Listing (arrowheads) shows the three cardinal axes: horizontal (y), vertical (z), and torsional (x), respectively. For example, horizontal recti rotate the eye mainly around the z -axis: lateral rectus, rightward (negative z); medial rectus, leftward (positive z). In Listing's frame of reference, Listing's plane coincides with the yz plane, and the x -axis points in the so-called primary direction.

emerge from the joint characteristics of our mechanical system and the proposed optimal control laws. Finally, in Section IX we discuss the achievements and directions for future research.

II. HUMAN OCULAR SYSTEM BACKGROUND

This section describes the anatomy and properties of the human oculomotor system that are essential to comprehend and validate our contributions. It also introduces the mathematical notation that will be invoked later.

A. Human-eye and Extraocular Muscles

The eye is enclosed within a conical cavity, where fat and connective tissues restrict its translation [16][17]. Thus, the eye can effectively only rotate with three degrees of freedom by actuating six extraocular muscles that control its orientation (see Fig. 1). The muscles in the horizontal plane of the right eye, the medial (MR) and lateral (LR) recti, rotate the eye mostly horizontally. The four muscles around the medial plane, the superior (SR) and inferior (IR) recti, along with the sideways pulling superior (SO) and inferior (IO) obliques, enable vertical and cyclo-torsional rotations. It is important to note that the pulling directions of the six muscles are not independent of each other and depend on the orientation of the eye [16]. As illustrated in Fig. 1, any 3D eye orientation can be obtained by rotations around the x , y and z axes, specifying *cyclotorsion*, *pitch* and *yaw*, respectively. Whereas yaw rotation is achieved by the LR-MR antagonists, pure pitch and cyclotorsional rotations require joint actuation of the four vertical-torsional muscles.

Recordings from primate oculomotor neurons have indicated that, with the eye at rest in the primary position, approximately 65% of the neural population is recruited [18]. Effectively, this means that the eye is kept under continuous pre-tension and that the neural control for eye movements modulates the relative innervation of agonist and antagonist muscles by changes in firing rates to enable high-precision angular control of the eye. In addition, in a cable-driven robotic

system, cables transmit force by applying tension and therefore must remain under tension at all times. To ensure the proper function of a cable-driven robotic eye and to prevent actuator backlash, the six cables must be pre-tensioned [19]. However, the amount of cable pre-tension must be adjusted with care: excessive pre-tension causes more friction, leading to faster wear and tear and shorter lifetime [20]. Insufficient pre-tension causes slack and deficiency in the control [19].

B. Saccade kinematics

Typically, humans make about 3-4 saccades per second to scan the visual environment [21] and these are constrained by *Donders' law*, which restricts the rotational degrees-of-freedom of the eyes from three to two [22]. Donders' law states that any eye orientation has a unique cyclotorsional angle, regardless of the path followed by the eye to reach that orientation. It has been argued that Donders' law avoids the problems associated with the non-commutativity of 3D rotations, which becomes especially important when planning sequences of eye and head movements [23][24][25]. *Listing's law* is a further specification of Donders' law. It provides an extra restriction on the eye's cyclotorsion for the special condition with the head upright and still, and the eyes looking at infinity. To describe 3D eye orientations, the neuroscience literature typically uses the Euler-Rodrigues rotation vector, $\mathbf{r} \equiv \tan(\rho/2) \cdot \hat{\mathbf{n}}$, where $\hat{\mathbf{n}}$ is the unit axis of rotation, and ρ the rotation angle that brings the eye from the reference orientation at $\mathbf{r} = \mathbf{0}$ to the current orientation [23][25][26]. In this representation, Listing's law constrains all eye orientations to Listing's plane, which in the laboratory frame (where $\mathbf{r} = \mathbf{0}$ is straight ahead) is described by $r_x = a \cdot r_y + b \cdot r_z$. A change of coordinates aligns Listing's plane with the (yz) plane, i.e., $r_x = 0$. In Listing's frame of reference, $\mathbf{r} = \mathbf{0}$ is the physiologically defined primary position (Fig. 1). Note that Listing's law holds not only during steady eye fixations but also during smooth-pursuit eye movements and rapid saccadic eye movements. It does not apply to eye-head coordination, static head tilts, vestibular and optokinetic stimulation, or for disjunctive vergence eye movements to fixate nearby targets, for which Donders' law applies [27].

C. Saccade dynamics

A further important property of saccades is their nonlinear dynamics, described by the so-called *main-sequence* [28]. In humans, the peak velocity of the saccade, V_{pk} , saturates at large amplitudes, A , which follows from the affine increase in the duration of the saccade, D , with A : $D = a \cdot A + b$. Because normal velocity profiles are single-peaked, there is a linear relation between A and $V_{pk} \cdot D$. Fig. 2 c-d shows schematic diagrams of these properties. Finally, behavioral experiments have shown that oblique saccade trajectories are approximately straight [29]. As a consequence, the horizontal and vertical component velocities are scaled versions of each other (i.e., they are synchronized), resulting in significant stretching of the smaller component's duration when it participates in an oblique saccade.

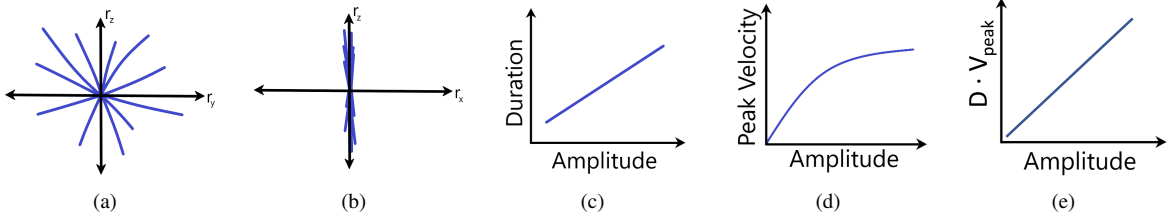


Fig. 2. Schematic illustration of human saccade kinematics (a,b) and nonlinear dynamic (c,d,e) properties. Panels (a) and (b) show the (r_y, r_z) and (r_x, r_z) views of the thin plane formed in 3D when eye orientations during saccades are represented by rotation vectors (Listings' law: $r_x = 0$). Note nearly straight trajectories in all directions (a). Panel (c) shows the affine relationship between saccade duration and amplitude. Panel (d) shows the saturation of peak eye velocities with increasing saccade amplitudes, while panel (e) shows the linear relation between saccade amplitude and duration times peak eye velocity.

TABLE I
COMPARISON OF OUR PROPOSAL WITH SIMILAR ROBOTIC EYE SYSTEMS AND SIMULATION MODELS

Model	Control DOF	Muscle type	Realistic muscle insertions	Saccade directions	Listing's Law	Main- Sequence
MACEYE[7]	4	Cables with motors	✗	✗	Mechanically enforced	✗
Rajendran et al.[30]	4	Contractile muscles	✗	✗	✗	✗
Wang et al. [31]	6	Pneumatic muscles	✗	✗	✗	✗
Lakzadeh, M. [32]	6	Cables with motors	✓	1D	✗	✗
Wei et al.[33]	6	Simulated muscle strands	✓	1D	✗	✗
Priamikov et al.[34]	6	Simulated Hill-type muscles	✓	1D	✗	✗
Iskander et al.[35]	6	Simulated Hill-type muscles	✓	1D	Implemented as constraint	✗
John, et al. [15]	3*	Cables with motors	✗	2D	✓	✓
Our paper	6	Cables with motors	✓	2D	✓	✓

DOF: Degrees of freedom.

* The robot in [15] had six muscles but were activated as pairs of hard-coupled motors.

III. RELATED ROBOTICS WORK

This section reviews those robotic eye models in the literature that have tried to replicate characteristics found in biology. These models have focused on achieving high movement speeds, or a human-like external appearance [36], [37], [38], or replicating prerecorded human gaze shifts [39], [40], [41], or hardcoding the biological control rules into the robot control system [42]. However, none of these models studied how the eye movements emerge and how they can be generalized to other designs, as every new design requires a new controller. Furthermore, typical robotic eyes are equipped with only 2 degrees of freedom (DOF), usually pan-tilt serial kinematics to control the yaw and pitch of gaze, and cannot independently control ocular cyclotorsion.

Some robotic eye designs made explicit links to the biological oculomotor system and its actuation [7], [43], [30], [44], [31], [32]. Canata et al. [7] developed a mechanical eye driven by four tendons (MAC-EYE). It complied with Listing's law (Section II) by implementing the appropriate routing of the four cables through precalculated pathways. Although a hardwired implementation of Listing's law seems an interesting engineering solution, it does not explain how this property emerges in the human oculomotor system. In [43], [30], a robotic eye is described, driven by four biologically more realistic contractile muscles. However, the chosen muscle attachments were not similar to those in the human eye. Wang et al. [31] developed a system with six Pneumatic Artificial Muscles (PAMs) with more realistic insertion points, but with the four recti muscles symmetrically arranged, unlike the human recti. The system developed in [32] had six cables with realistic insertions and pulling directions. However, their eyeball did not rotate around a fixed spherical joint but within a nested gimbal. As the system's inertia changes when

moving, it is ineffective for studying saccade dynamics. None of these robotic eyes were used to study oblique saccade trajectories, the *main-sequence* relationships, and underlying muscle-control signals.

Some studies aimed to model the complete complexity of extraocular muscles through simulation [33], [34], [35]. These studies used inverse dynamics or neural activation patterns to drive the simulated eye in a saccade-like way, but they were all limited to 1D behaviors. Although this may help to understand certain clinical deficits, the complexity of the model impedes the application of different control strategies that could lead to the stereotypical kinematic and dynamic properties of human saccades.

A comparison of previous work on robotic eyes is summarized in Table I. Two of these systems [7], [30] were restricted to four muscles only, and two others [15], [31] did not implement accurate muscle pulling directions. For a proper understanding of the 3D oculomotor system, however, it is important to model the coupled pulling actions of all six muscles in 3D, and thus account for the considerable nonlinearities in the system. Although some studies model the human eye in high detail in a simulation environment [33], [34], [35], or with thoroughly scaled physical features [32], they only show saccade-like movements in the horizontal or vertical directions, and did not employ the full 3D coordination of the system, or saccades in oblique directions. To the best of our knowledge, no study modeled the control of the full 3D system with six muscles to understand the emergence of Listing's Law, the stereotypical *main-sequence* behavior, and straight oblique trajectories of fast saccades.

It has been hypothesized that the brain may optimize a certain cost function, which would lead to the saccadic properties of Fig. 2. However, the application of optimal control theory

to understand the emergence of human saccadic behaviors has so far been confined to 1D [12], or decoupled 3x1D models [13]. For example, [14] studied how open-loop optimal control, combined with a local learning mechanism, could generate eye-head movements in a 1D linear model.

We recently tested a feedforward open-loop optimal control strategy [45], based on a linear approximation of a simple, but non-linear, 3 DOF unconstrained biomimetic robotic eye, which reproduced the 3D dynamics and kinematics of human saccades [15]. The biomimetic eye had three independent motors, hard coupled to agonist-antagonist cable pairs. The linear approximation for the open-loop controller applied system identification on a physics-based robot simulator. Despite its realistic behaviors, the inherently fixed hard coupling of agonist-antagonistic pairs is an unrealistic feature, which does not explain how it actually emerges in the biological oculomotor system, where the six muscles are independently controlled by their own motor-neuronal nuclei[46], [47], [48], and where agonist-antagonist pairing is a dynamic and flexible strategy that depends on changes in 3D eye orientation[16], [49], [50].

IV. PROBLEM DEFINITION

We here propose a novel robot design for a realistic 6 DOF biomimetic eye. To better understand its control and to enable a full characterization of the system, we developed a numerical simulator. Compared to the 3 DOF model in [15], our new 6 DOF actuation system brings additional challenges. In particular, the control has to resolve the agonist-antagonist coupling of the muscles and set the appropriate muscle pre-tensions, which impact on the highly redundant muscular system. For this new system, we developed a controller that replicates most of the kinematic and dynamic characteristics of human saccades, including the emergence of an agonist-antagonist organization of distinct muscle pairs according to the basic optimality criteria.

Similarly to our previous work [15] we take a model-based stance to the control problem, which we divided into two steps: deriving forward models of the mechanical eye, suitable for control design (*Problem 1*), and computing open-loop optimal control trajectories for the modeled system (*Problem 2*).

Problem 1 (Approximating the forward dynamic model): To obtain suitable control trajectories with reasonable computational resources, we need to create fast models that approximate the dynamic equations based on nonlinear physics of the cable-driven robotic eye system of Fig. 3. We represent the motor angles as $\mathbf{u} \equiv [u_{IR}, u_{MR}, u_{SR}, u_{LR}, u_{IO}, u_{SO}]^T$ and the 6 DOF eye state is composed of its 3D orientation and angular velocity: $\mathbf{x} \equiv [r_x, r_y, r_z, \omega_x, \omega_y, \omega_z]^T$. In [51] we computed linearized approximations of the system equations. However, analytic linearization methods are quite tedious and hard to extend to future model improvements. In this work, we trained a nonlinear neural network model to approximate the system dynamics and used it in the optimization of the control trajectories. The next state of the system, \mathbf{x}_{t+1} , is predicted from the control input \mathbf{u}_t for the 6 motors and the current state \mathbf{x}_t , where t indicates discrete time. Thus, the model could be

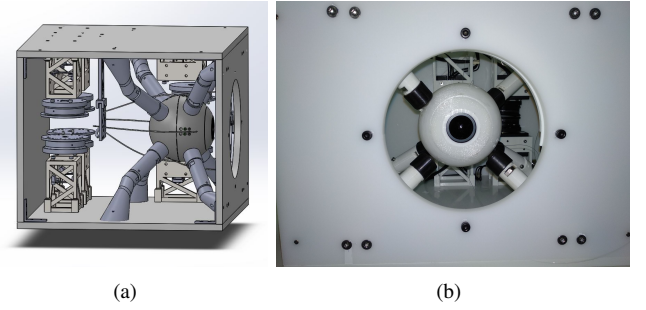


Fig. 3. (a) Schematic 3D side view of our biomimetic human eye prototype, with six motors (five spindles are visible) independently controlling the six cables ('extraocular muscles'; four are visible) connected to the eyeball. The eye is held in place by eight external arms to allow only 3D rotations around its fixed center. The ball-contacts of these arms on the eye (not visible) provide a dynamic frictional force that increases the total damping. (b) Front view of the actual mechanical prototype showing the eye with the camera.

defined by the evolution of the state, under the action of the command: $\mathbf{x}_{t+1} = \mathbf{f}(\mathbf{x}_t, \mathbf{u}_t)$.

Problem 2 (Trajectory optimization): We are attempting to generate saccades that have similar characteristics to those of humans, across the entire 3D range, by formulating the saccade generation process as an optimization problem with various criteria. The optimal trajectory, $\mathbf{u}_{0:T}^*$, brings the eye from the initial state, \mathbf{x}_0 , to its final state, \mathbf{x}_T , in a finite time-interval, $t \in [0, T]$.

If we consider $\mathbf{u}_{0:T} = [\mathbf{u}_0, \mathbf{u}_1, \dots, \mathbf{u}_T]$ as the sequence of input motor commands, then the problem is to find those input motor commands that generate the optimal trajectory at a minimum cost. This cost is typically composed of a linear combination of partial costs on the properties of the trajectory, e.g. *duration*, *accuracy*, *energy*. The optimal control problem can thus be written as:

$$\begin{aligned} \min_{0 \leq T \leq T_{\max}} \left(\min_{\mathbf{u}_{0:T}} \sum_{t=0}^T C(\mathbf{x}_t, \mathbf{u}_t, T) \right), \\ \text{subject to : } \mathbf{x}_{t+1} = \mathbf{f}(\mathbf{x}_t, \mathbf{u}_t), \quad \mathbf{u}_t \in \mathcal{U} \end{aligned} \quad (1)$$

where, $C()$ indicates the cost of input state \mathbf{x} and motor command \mathbf{u} for a given duration T , T_{\max} is a bound on the possible values of T , and \mathcal{U} is the set of feasible commands. The optimization process is generally organized in an inner optimization of the motor commands \mathbf{u} for a fixed time horizon T , and an outer loop that optimizes T in a certain range $0 \leq T \leq T_{\max}$. Details about the components of the cost function are provided in Section VII.

V. DESIGN OF THE 6 DOF CABLE-DRIVEN ROBOTIC EYE

Figure 3 shows the 3D model and the mechanical prototype of our system. Like the human eye, the robotic eye rotates with 3 DOF around its fixed center whenever the six elastic cables, which represent the extraocular muscles, exert a net torque. Cables are inserted into the globe at contact points (Table II), which were scaled and slightly adjusted from human measurements [52]. Each cable is controlled by its own motor that rotates at a given speed, which pulls the cable around its spindle to exert a torque on the eye. Because cable pulling

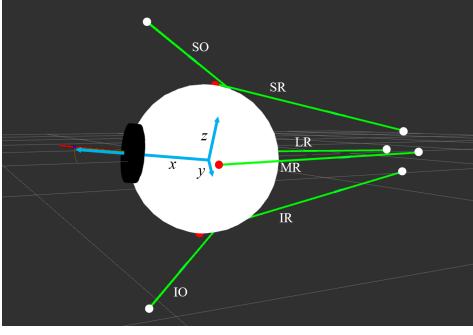


Fig. 4. Visualizaton of the extraocular muscles (green) for the simulator of the right eye, deviated to the right (red line) from straight-ahead (light blue laboratory frame), where red and white dots indicate insertion points on the eye and head, respectively. Note that the cable pulling directions are not symmetric to the center of the eye, because the insertion points on the head at the back are medially shifted in the $+y$ direction. As a result, the MR muscle is shorter than the LR when the eye is in the primary position.

directions vary with eye orientation and muscles can only pull (not push), the total system (described below in more detail) is *nonlinear* [15]. Thus, rotating the robotic eye in the same way as the human eye during saccades (i.e., accurately and at high speeds) becomes a highly nontrivial problem.

TABLE II
LOCATIONS OF CABLE INSERTIONS AT EYE AND HEAD.

Muscles	IR	SR	MR	LR	IO	SO
Insertion(eye)						
x(mm)	-2	-2	7.7	7.7	-11.2	-11.8
y(mm)	-1.4	0.8	39.3	-39.3	-1.4	-1.2
z(mm)	40	-40	0	0	38.3	-38.1
Insertion(head)						
x(mm)	-100.1	-100.1	-100.1	-100.1	45	45
y(mm)	40.7	40.7	51.6	29.6	37.5	37.5
z(mm)	7.8	-14.9	-3.5	-3.5	62	-62
Length(mm)	111.5	108.8	108.6	127.9	72.3	72.7

To study the properties and behavior of the biomimetic eye, we developed a simulator, in which the eye was modeled as a sphere with a fixed center, subject to Newton-Euler's rigid body equation of angular motion, and actuated by the six cable-driven actuators:

$$\boldsymbol{\alpha} = \mathbf{I}^{-1}(\boldsymbol{\tau}_{net}(\mathbf{x}, \mathbf{u}) - \boldsymbol{\omega} \times \mathbf{I}\boldsymbol{\omega}) \quad (2)$$

where $\boldsymbol{\alpha}$ is the eye's angular acceleration, \mathbf{I} is the inertia tensor of the eye, \mathbf{u} is the motor configuration of the 6 motors, $\boldsymbol{\omega}$ is the eye angular velocity, \times denotes the vector (cross) product, and $\boldsymbol{\tau}_{net}$ is the net torque on the eye, which depends on the dynamic friction and elasticity torques, $\boldsymbol{\tau}_d$ and $\boldsymbol{\tau}_k$:

$$\boldsymbol{\tau}_{net} = \boldsymbol{\tau}_k + \boldsymbol{\tau}_d = \sum_{m=1}^6 \boldsymbol{\tau}_m - \mathbf{D}\boldsymbol{\omega} \quad (3)$$

Here, \mathbf{D} quantifies the eye's damping matrix, subscript m is the motor index, and the torque exerted by each muscle is

$$\boldsymbol{\tau}_m = \mathbf{Q}_m \times \mathbf{f}_m \quad (4)$$

where \mathbf{Q}_m is each muscle's insertion point on the eye, and \mathbf{f}_m is the force applied by each muscle on the eye, which depends on the current state \mathbf{x}_t , goal state, \mathbf{x}_G , and control input \mathbf{u}_t .

To simplify the modeling, the cables were approximated by linear elastic springs. The elastic force applied to the eye by each cable (\mathbf{f}_m) then depends on its length (l_m), determined by the sum of the length of the cable wound to the motor spindle and the length between the fixed cable head-routing point (white dots in Fig. 4) and the final contact point on the eye (red dots). The length of the cable for each muscle (l_m) varies with the rotation of the motors (\mathbf{u}) and the orientation of the eye (in state \mathbf{x} ; we omit the time index t , for clarity),

$$l_m(\mathbf{x}, \mathbf{u}) = \|\mathbf{Q}_m(\mathbf{x}) - \mathbf{P}_m\| + r_{sp} \cdot u_m \quad (5)$$

with \mathbf{Q}_m and \mathbf{P}_m the (eye and head) insertion points of cable m , r_{sp} the radius of the spindle, and u_m the rotation angle of the spindle for cable $m \in \{IR, MR, SR, LR, IO, SO\}$. This leads to a dynamic elastic force that is determined by Hooke's law [53]:

$$\mathbf{f}_m = \frac{k}{l_{0m}}(l_m(\mathbf{x}, \mathbf{u}) - l_{0m})\vec{\phi}_m \quad (6)$$

where k is a constant depending on the material and thickness of the cables and l_{0m} is the rest length of cable m . $\vec{\phi}_m$ is the unit vector in the direction of the force applied to the eye.

The inertia of the eye ($\text{diag}(\mathbf{I}) = [4.8, 4.3, 4.8] \times 10^{-4}$ kg·m²), muscle stiffness ($k = 20$ N) and damping parameters ($\text{diag}(\mathbf{D}) = [0.04, 0.04, 0.04]$ Nms), were selected to closely replicate the biomechanics of the human eye [21]. To implement the constraint that the elastic cables can only pull, the force was set to zero as soon as it went negative. When this happens, the cable loosens and no longer applies tension, a phenomenon known as *slack* (see VII-C). Note also that since the constant of elasticity, k , was taken identically for all cables, the effective stiffness varies for movements in different directions. For example, for horizontal movements, the elastic forces are primarily delivered by LR and MR, but vertical movements involve the interaction of SR, IR, SO, and IO.

VI. APPROXIMATIONS OF THE SYSTEM DYNAMICS

The computation of optimal commands through (1) could ultimately be done with non-linear optimization techniques applied to the non-linear physics simulator of the eye system. However, running the non-linear physics simulator in the optimization loop is too time-consuming due to the integration of the non-linear differential equations. In a previous work, our team explored a local derivative-based linearization of the non-linear system dynamics, by applying an infinitesimal perturbation method around an equilibrium point [54]. The linear model proved to accurately approximate the nonlinear system for small perturbations around the linearization point, but the quality of the approximation quickly degraded for large saccades. Furthermore, the analytic linearization method involves nontrivial derivatives and does not scale well with physical model complexity. Therefore, in this work, we opt to use a nonlinear data-driven method that learns an approximation of the model from samples of input-output data. This method is much faster to compute than the physics-based simulation and can be adapted to variations of the system by relearning the model after acquiring new input-output data sequences.

The *nonlinear autoregressive network with exogenous inputs* (NARX) is a type of recurrent neural network [55], [56] that has been applied to model the complex dynamics of nested manipulators [57].

In discretized time, the NARX model can be written as: $\mathbf{x}_{t+1} = f(\mathbf{x}_{t-n_x:t}, \mathbf{u}_{t-n_u:t})$ where the next value of the dependent output signal \mathbf{x}_{t+1} is regressed on previous values of the same output signal $\mathbf{x}_{t-n_x:t}$ and previous values of an independent (exogenous) input signal $\mathbf{u}_{t-n_u:t}$. We have adopted the MatlabTM implementation for the NARX model, illustrated in Fig. 5.

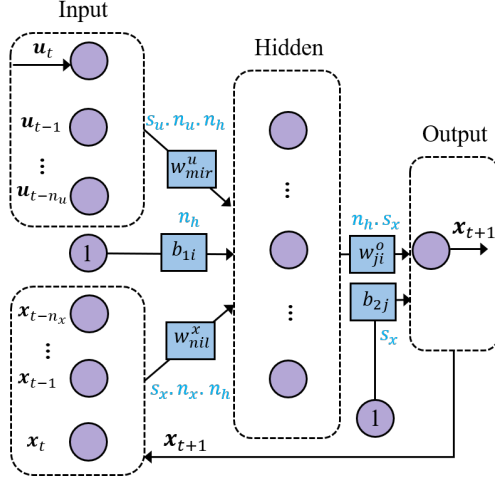


Fig. 5. Architecture of the fully-connected NARX model with input, hidden, and output layers. Number of hidden units, $n_h = 55$; input memory: $n_u = 1$; $n_x = 3$; DoF of the state: $s_x = 6$; DoF of the input: $s_u = 6$.

In summary, the NARX model takes the current and past motor commands, $\mathbf{u}_{t-n_u:t}$ and the current and past state, $\mathbf{x}_{t-n_x:t}$ from the nonlinear system as input to predict the state for the next time step. The size of the network's memories of control commands and states is $n_u + 1$ and $n_x + 1$, respectively. In Fig. 5, n_h is the number of neurons in the hidden layer; s_x and s_u are the sizes of the input vectors \mathbf{u} and \mathbf{x} , respectively. $\mathbf{u}_{t-n_u:t}$ and $\mathbf{x}_{t-n_x:t}$ are the (past) inputs to the network. \mathbf{x}_{t+1} is the output of the network. $b_{1,i}$ and $b_{2,j}$ are the bias weights for the hidden layer and the output layer, respectively. The weights w_{mir}^u connect the input to the hidden layer, w_{ji}^o connect the current and past states to the hidden layer, and w_{ji}^o connect the hidden layer to the output layer ($i \in [1, n_h]$, $j \in [1, s_x]$, $m \in [1, s_u]$, $r \in [1, n_u]$, $l \in [1, n_x]$).

The output of each layer is computed by applying nonlinear (sigmoid) (f_1) and linear (f_2) activation functions, respectively. The biases and weights of the network are adjusted during network training using the *Levenberg-Marquardt back-propagation* technique.

The output of neuron i at time t in the hidden layer, $H_i(t)$, is computed by:

$$H_i(t) = f_1 \left(\sum_{m=1}^{s_u} \sum_{r=n_u}^0 w_{mir}^u \mathbf{u}_{t-r}^{(m)} + \sum_{j=1}^{s_x} \sum_{l=n_x}^0 w_{jil}^x \mathbf{x}_{t-l}^{(j)} + b_i \right) \quad (7)$$

where the notation $\mathbf{u}^{(k)}$ indicates the k th entry of vector \mathbf{u} . The output of the network is determined by:

$$\mathbf{x}_{t+1}^{(j)} = f_2 \left(\sum_{i=0}^{n_h} w_{ji}^o H_i(t) + b_j \right). \quad (8)$$

VII. OPTIMAL CONTROL

A. The Cost Function

Saccades should reach the goal as fast and as accurately as possible, while consuming the least amount of 'metabolic' resources, i.e., energy. This leads to the inclusion of three cost functions in the optimal control. In our previous study [15], we did a comprehensive analysis of different combinations of costs and found that the following costs are the most important for generating human-like saccades.

1. *Duration cost* (J_D): *Saccade duration* quantifies the time, T , the eye needs to move from initial to final state: the longer, the higher the cost, as saccades should reach the goal in minimum time. The duration cost, $J_D(T)$, is defined by a hyperbolic discount function [15], [45], [58]:

$$J_D(T) = 1 - \frac{1}{1 + \beta T} \quad (9)$$

2. *Accuracy cost* (J_A): Importantly, the eye should reach the goal state \mathbf{x}_G at time T as accurately as possible, and at zero velocity and acceleration if the target is not moving. We took the accuracy cost, J_A , as the Euclidean norm of the difference between the final 3D eye state reached by the controller and the desired goal with zero torsion, $\mathbf{x}_G = (0, G_y, G_z, 0, 0, 0)$. Since the primary position is not known a priori, we expressed the 3D accuracy cost in laboratory coordinates. We also included a penalty for any state change in a window of $W = 5$ samples as soon as the eye reached the goal at time T :

$$J_A(\mathbf{x}) = \sum_{t=1}^W \|\mathbf{x}_G - \mathbf{x}_{T+t}\|^2. \quad (10)$$

3. *Energy cost* (J_E): We assume that the total energy consumption by the saccade is proportional to the actuators' angular velocities. As the time steps are uniform, angular velocities can be approximated by differences between angular positions. The energy cost, J_E , is thus written as [45]:

$$J_E(\mathbf{u}) = \sum_{t=1}^T \|\mathbf{u}_t - \mathbf{u}_{t-1}\|^2 \quad (11)$$

B. Controller Design

To reduce the computation effort of the optimization, we represent the sequence of input motor commands $\mathbf{u}_{0:T}$ of a saccade trajectory as a weighted sum of normalized Gaussian basis functions, $\varphi^i(t)$. The configurable number of basis functions, N , can be much smaller than the number of time steps in the trajectory. Formally,

$$\mathbf{u}_t = \sum_{i=1}^N \mu_i \varphi^i(t), \quad \varphi^i(t) = \frac{\exp \left[- \left(\frac{t-c_i}{h} \right)^2 \right]}{\sum_{m=1}^N \exp \left[- \left(\frac{t-c_m}{h} \right)^2 \right]} \quad (12)$$

where μ_i are 6×1 coefficient vectors that will be returned by the optimization process instead of \mathbf{u}_t . For a saccade with duration T , we take $N = \gamma T$ Gaussian basis functions (with $\gamma < 1$ for effective computational reduction), with centers c_i , that are evenly spaced ($\Delta c = T/(\gamma T - 1) \approx \gamma^{-1}$) and with a common standard deviation $h = 2\Delta c$ to ensure good coverage of the temporal dimension. This roughly corresponds to a fixed partition of the duration range.

Defining a $6 \times N$ matrix, $\mathbf{M} = [\mu_1 \cdots \mu_N]$, and a $N \times (T + 1)$ matrix, $\Phi = [\varphi_{0:T}^1; \cdots; \varphi_{0:T}^N]$, where $\varphi_{0:T}^i$ is the vector with the samples of the i th normalized Gaussian taken at the discrete times, the control trajectory can be written as: $\mathbf{u}_{0:T} = \mathbf{M}\Phi$. Therefore, instead of finding $6 \times (T + 1)$ values for a trajectory $\mathbf{u}_{0:T}$, we only need to compute the $6 \times N$ entries from \mathbf{M} , where $N < T$.

The entire trajectory optimization in (1) is done as a bilevel optimization. The duration of the saccade T is optimized in the outer loop of (1). For a selected T , the inner optimization problem can thus be written as

$$\begin{aligned} \mathbf{M}^* &= \underset{\mathbf{M}}{\operatorname{argmin}} J(\mathbf{x}, \mathbf{u}, T) = \sum_{\alpha \in \{D, A, E\}} \lambda_\alpha J_\alpha(\mathbf{x}, \mathbf{u}, T) \\ \text{subject to: } &\mathbf{x}_{t+1} = f(\mathbf{x}_t, \mathbf{u}_t), \quad t = 0, 1, \dots, T \\ &\mathbf{u}_{0:T} = \mathbf{M}\Phi, \quad \mathbf{u}_t \geq 0 \end{aligned} \quad (13)$$

where each cost term, J_α , is multiplied by a fixed weight λ_α and the next state, \mathbf{x}_{t+1} , is computed by the nonlinear NARX model equation in Section VI. Fig. 6, shows how the trajectory is generated by the inner optimization loop

One of the challenges in optimization is to set appropriate values for the cost weights λ_α . We first estimated the range of candidate values, after which, by trial and error, we manually found the appropriate values for the λ 's.

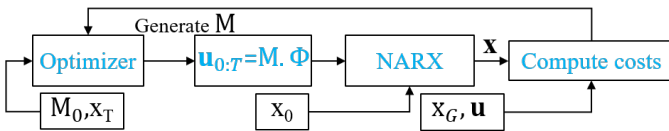


Fig. 6. In the nonlinear optimal control approach, the optimizer generates μ and thus \mathbf{u} as input for the NARX model. From the NARX output, the cost is calculated according to the optimization scheme (13).

The optimization procedure, including the inner and outer optimization of (1), is summarized in Alg. 1. Initially, the parameters λ , d (number of saccade durations to be evaluated) and γ (ratio of the number of basis functions with respect to the saccade duration in ms) are set. The initial and desired orientations of the eye ($\mathbf{x}_0, \mathbf{x}_G$) are taken as input. Then, for the possible d saccade durations in $0 < T_j \leq T_{\max}$, it computes the optimal motor controls and the cost of that solution. Finally, the duration with the lowest cost is the optimal duration T^* . We applied MATLAB's function *fmincon* with the 'sqp' solver to optimize (13). In our experiments, the following values were set: $d = 10$, the maximum number of iterations for the solver was set to 15, and $\gamma = 0.24 \text{ ms}^{-1}$, which corresponds to a separation between Gaussians of about 4.2 ms and a standard deviation of 8.6 ms . These parameters

Algorithm 1: *Trajectory_Optimization()*

```

param ← λ, d, γ Initialize parameters
Input: x_0, x_G Initial and final orientation
for j = 1 to d do
1  T_j ← j * T_max / d Saccade duration
2  N_j ← γ * T_j Number of basis functions.
3  Φ_j ← GBF(N_j, T_j) Create Φ_j.
4  M_j^0 ← CreateMuZero(N_j) Initialize M_j.
5  [cost_j, M_j] ← Optimise(J(x_0, x_G, M_j^0, Φ_j, λ)
    Optimize cost with given parameters.
6 [T*, M*, Φ*] ← min(cost_j) Find optimum values.
7 u* ← M* · Φ* Optimal trajectory.
  
```

were empirically tuned for a good trade-off between computational time reduction and accuracy. We further restricted the maximum duration of the saccade to $T_{\max} = 210 \text{ ms}$ and initialized all elements of the matrix \mathbf{M} at 2 (corresponding to the resting position and all six motors with fixed pretension).

C. Controlling pre-tension

Because of the redundancy in controlling the 3D orientation of the eye with 6 motors, the same orientation can be achieved by (infinitely many) different motor-angle combinations, as the amount of co-contraction of antagonistically acting muscles is undetermined. Therefore, an important feature to control is the amount of pre-tension (the set of initial motor angles), such that the eye is able to reach any orientation in the oculomotor range without the cables going slack during eye movements. Therefore, we optimized the initial motor angles (\mathbf{u}) such that their squared norm is minimal, under the constraints that ensure positive cable forces in equilibrium state \mathbf{x} , while the total elastic torque in the system is zero ((3) and (6)):

$$\begin{aligned} \min_{\mathbf{u}} \quad & \|\mathbf{u}\|^2 & \mathbf{f}(\mathbf{x}, \mathbf{u}) &> 0 \\ \text{subject to} \quad & \tau_k(\mathbf{x}, \mathbf{u}) = 0 \\ & \mathbf{u}_{\text{agonist}} + \mathbf{u}_{\text{antagonist}} > 2\theta \end{aligned} \quad (14)$$

where \mathbf{f} if the tension at each cable, τ_k is the total torque resulting from the cable tensions, and θ is a minimum bound for the average motor angle for the three antagonistic motor pairs ($\mathbf{u}_{\text{agonist}}$ and $\mathbf{u}_{\text{antagonist}}$). These pairs are MR-LR, IR-SR, and IO-SO. The value of θ is a user-defined parameter that depends on the radius of the spindle around which the cables are wound and should be chosen as the lowest value for which the cables would not move slack throughout the trajectory.

Note that we did not control for slack explicitly at runtime. Our strategy to prevent slack was to empirically tune the pretension of the tendons such that we would not observe slack in a set of large saccades. As we have not verified the existence of slack in all other saccades tested, we cannot theoretically ensure the absence of slack for all cases.

VIII. SIMULATION RESULTS

To evaluate our approach, we analyzed and compared several output parameters of the system regarding the 3D

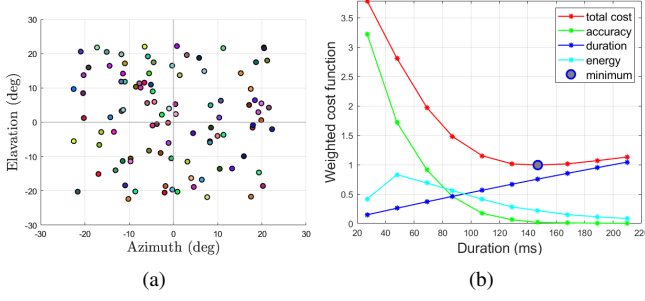


Fig. 7. (a): The 99 oblique goal directions as azimuth (rightward positive) and elevation (upward positive) angles in the amplitude range from 5 to 30 degs, as used for the zero-initial and continuous saccade tests in our experiments. (b): Cost functions for a rightward horizontal saccade of 22° starting from the origin in the trajectory optimization procedure, evaluated at 10 discrete time steps. The large blue dot indicates the minimum total cost of the trajectory, and is found at $T = 147$ ms.

kinematic (Listing's plane) and dynamic (velocity profile) behavior (Fig. 2), and the 'neural' control signals from the six motors.

A. Simulation Setup

To evaluate our controller on saccades of different amplitudes and directions, we created a test set of 99 random target locations in horizontal, vertical, and oblique directions with amplitudes between 5 and 30 degrees from straight-ahead (Fig. 7a). We performed two saccade sequences: a *zero-initial* sequence, where every saccade started from the origin $([0, 0, 0])$, and a *continuous* sequence, where the next saccade started from the final orientation of the previous saccade, and so on. All simulations were performed in *MATLAB 2021* on a laptop with *Windows 10* operating system, *16GB Ram* and a *CPU core i7*.

The weights λ_α of the three cost functions, J_α in our optimization (13) were manually calibrated with the aim to achieve human-like dynamic characteristics for the eye system: $\lambda_A = 1$, $\lambda_D = 0.04$ and $\lambda_E = 0.002$. Fig. 7b shows an example of the behavior of the three costs for a 22 deg horizontal saccade, together with the total cost (red), executed for ten different saccade durations between 30 and 210 ms. The optimal saccade duration, T , is found at the minimum of the convex total cost curve, that is, at $T = 147$ ms.

As for the setting of the cables' pre-tensions discussed in VII-C, we found by trial and error that values of θ around 2 radians (14) worked well for all saccades.

B. Model Learning

To train the NARX network, we have acquired a large sequence of input-output data sampled at a frequency of 1 ms. We have followed the approach of [15] and generated for input data independent pseudo-random binary signal sequences (PRBS) [59], typically used in system's identification. PRBS is a deterministic signal composed of rectangular pulses of fixed amplitude but variable duration that has properties similar to those of white noise (flat spectrum). Thus, it equally excites all frequencies of interest in the system. The amplitude range of

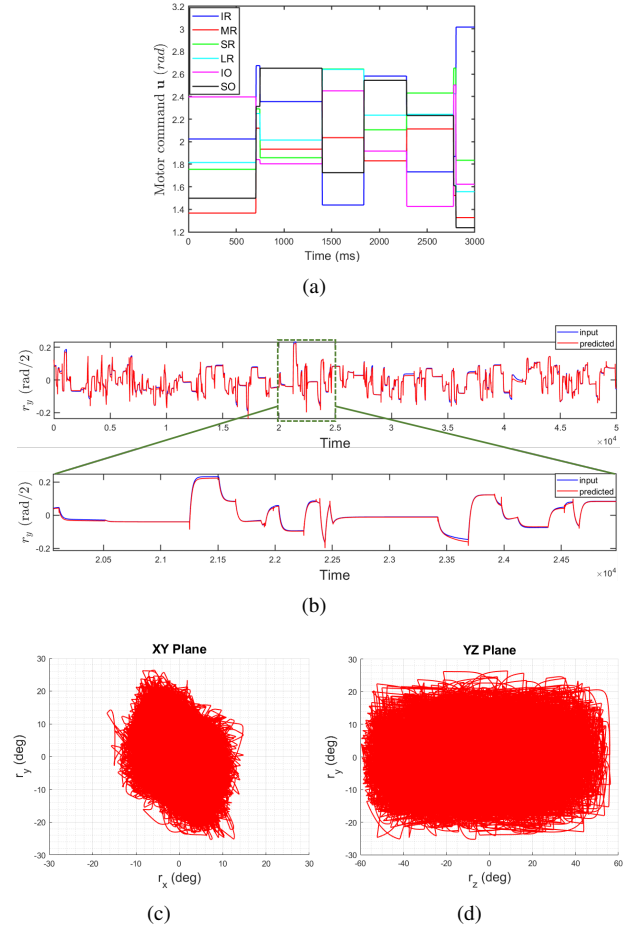


Fig. 8. (a): An illustrative selected section of random motor responses over 3000 ms (out of 2×10^6 ms), which served as a training set for the NARX network. Motor commands are within the range $[0-3]$ radians. (b): Eye orientation along the y -axis for a sample input signal (blue trace) of 50,000 samples (150,000 ms) and the predicted signal (red) for the trained NARX model. Inset: same data on an expanded scale. RMSE = 0.06 rad/2 and $r^2 = 0.97$ between data and prediction, indicating an excellent approximation. (c,d): Rotation vector components (in degrees) in the (xy) (c) and (yz) (d) planes of the corresponding 3D eye orientations in the laboratory frame (subsample of the total data set). Note that the $r_x r_y$ range of the system is smaller than the r_z range and that the data are slightly tilted in the xy plane.

these signals was chosen to obtain good approximations of the model output in the range of the desired saccade amplitudes.

The total data length is 2×10^6 ms, which covers a wide range of the workspace (Fig. 8). For computational reasons, we reduced the data size by downsampling the signals to 3 ms time intervals.

By feeding the data set to the NARX model, the best result was achieved after 96 training epochs with MSE = 0.0018 $(\text{rad}/2)^2$. Figure 8 shows the result of the trained NARX network (red line), tested on a random set of eye movements (blue trace), which verifies how well the network learned the forward dynamics of our non-linear robotic eye model.

C. Kinematic behavior

To study the 3D kinematics of the eye movements resulting from our controllers, we analyzed the amount of cyclotorsion of the 3D trajectories with respect to Listing's

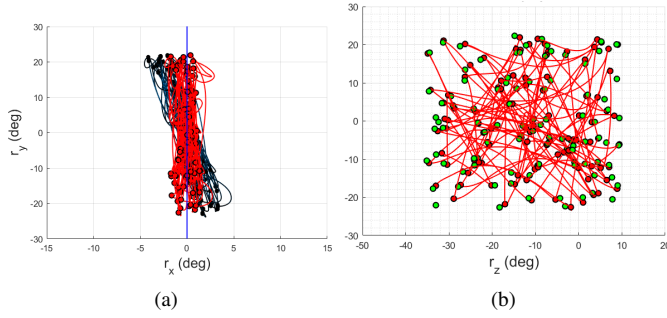


Fig. 9. (a) xy and (b) yz projections of 3D eye-movement trajectories in Listing's coordinates (red) from the continuous saccade sequence. Black: xy data in the laboratory frame before applying a rightward rotation of 18.11 deg about the z -axis into Listing's coordinates. The blue vertical line at $r_x = 0$ indicates Listing's plane after rotation. Green dots in (b) correspond to the actual (rotated) goals of the saccade set in Listing's frame (note different scales for the abscissas).

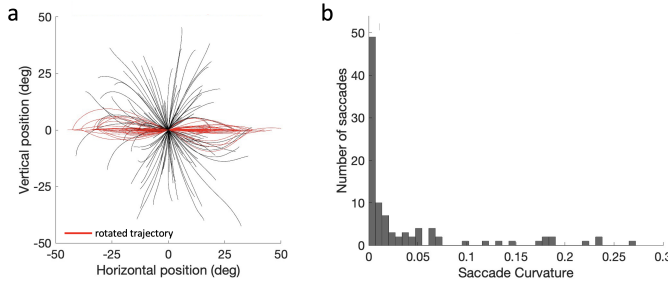


Fig. 10. a) Movement trajectories in vertical and horizontal direction for the 99 saccades of the random sequence, all aligned in (0,0) (black), and after their rotation onto the horizontal axis (red). b) The distribution of curvature values for all 99 saccades. The far majority of saccades is straight ($C < 0.03$).

plane. Fig. 9a shows the result of the continuous saccade test in the laboratory xy plane (black). Note that Listing's plane is, typically, not aligned with the vertical axis of the head frame. The data (red) were therefore rotated around the z -axis (after calculating the best-fit plane) to align them with Listing's frame of reference (cf. Fig. 2b).

Table III presents the standard deviations of cyclotorsion around Listing's plane for different amplitude ranges and saccade tests. These values correspond well with the range reported for monkey and human eye movements (between 0.6 and 1.0 deg) [23], [25].

Figure 9b shows the eye-movement trajectories in Listing's yz plane. Overall, the eye-movement trajectories appear quite straight.

To better quantify this observation, we calculated curvature, C , as the maximum absolute deviation, d_{max} , of the trajectory from the straight vector connecting the start and end points in the yz -plane, normalized by its vector length: $C \equiv d_{max}/|A|$ (e.g., for a semicircular trajectory, $C = A/(2A) = 0.5$) [60]. In Fig. 10a we show the set of continuous saccades of Fig. 9 after subtracting their starting points such that all trajectories align with the origin. Then, by rotating the trajectories to the horizontal axis the curvature simply becomes

$$C = \frac{\max(|v_t|)}{|h_{end} - h_{start}|}$$

TABLE III
STANDARD AND MAXIMUM DEVIATION OF THE LISTING'S PLANE.

Saccade/ Control	Saccade Amplitude ^o	Deviation (STD, Max) ^o
Zero-initial	< 10	0.12, 0.35
	< 20 & ≥ 10	0.24, 0.77
	< 35 & ≥ 20	0.36, 1.35
Continuous	< 10	0.52, 1.24
	< 20 & ≥ 10	0.54, 2.1
	< 35 & ≥ 20	0.85, 2.8

with v and h the vertical and horizontal coordinates of the rotated trajectory, respectively. Fig. 10b shows the distribution of saccade curvatures, C . We divided saccades into two main categories: straight ($C < 0.03$) vs. substantially curved ($C > 0.1$), and found that 70/99 saccades were straight, with only 6/99 substantially curved. This small group of curved saccades was generated from eccentric initial positions with saccade vectors not directed toward the center of the oculomotor range.

The straightness of saccade trajectories requires that the horizontal/vertical components of their velocity profiles are scaled: $\omega_H(t) \propto \omega_V(t)$. We indeed found high correlations (for the continuous saccade set: $\mu = 0.80$, $\sigma = 0.29$, see Table IV). As curvature was not explicitly included as a cost in our algorithm, this apparent cross-coupling in eye behavior is an emerging property of the optimal control strategy. However, this also must indicate a considerable amount of cross-coupling between the six motors, despite the fact that they are physically independent of each other. £1

D. Saccade accuracy

The absolute localization error of the saccades resulted to be independent of their amplitude, and was on average 1.47 deg (σ : 0.81 deg; see Fig. 11a; data from the nonlinear simulator). The relative error (absolute error normalized by amplitude) thus decreased with the saccade amplitude, in contrast to what has been reported for results obtained from human saccades [61] (see Discussion IX).

To analyze the source of the localization errors, we compared the accuracy of the solutions for the optimal trajectories obtained with the NARX model with those from the non-linear simulator. As the nonlinear simulator represents the actual physical plant, any errors in the accuracy of the end points must be due to the trade-off between *accuracy*, *duration*, and *energy*, expressed in the optimization cost function (apart from numerical errors). The results are illustrated in Fig. 11. Panel 11b shows the oblique saccade trajectories for the zero-initial data set in laboratory coordinates for the simulator (red) and NARX (blue), which shows that, despite some small non-systematic discrepancies, the trajectories are highly similar. The green dots show the target locations. Panels 11c,d compare the horizontal and vertical localization error components for the two approximation methods. Both methods yielded small errors (typically below 2 deg), and both component errors were correlated. Overall, the NARX model provided a good approximation for the nonlinear physics-based simulator, and did not add systematic errors to the accuracy of the solution.

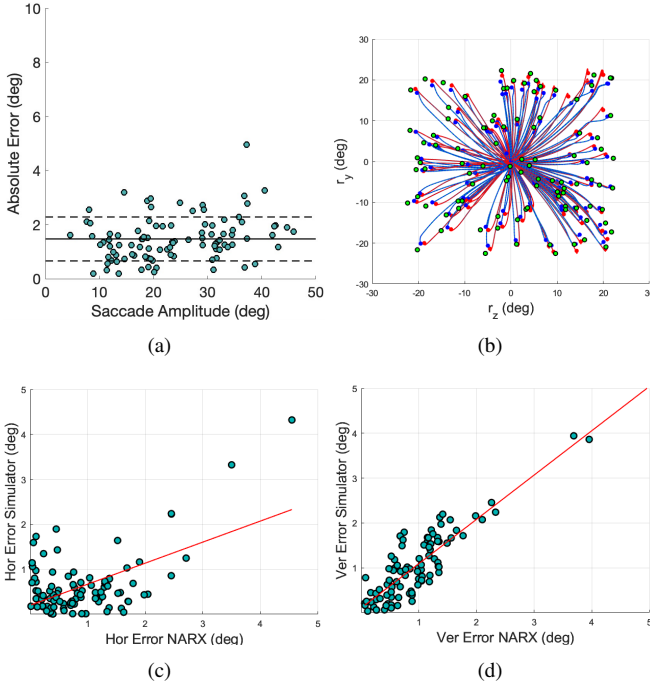


Fig. 11. Accuracy. (a) The absolute localization errors (distance between target and saccade endpoint), here shown for the continuous saccade set versus the saccade amplitude of the nonlinear simulator. Note that errors do not systematically increase with saccade size. Mean error: 1.47 deg (σ : 0.81 deg). (b) yz plane of the zero-initial saccade trajectories for the nonlinear simulator (red) and NARX model (blue). Green dots are the target points. Note the similarity between the two approximation methods. (c) Comparison of the endpoint localization errors of the horizontal target component generated by NARX and Simulator. (d) Comparison of the localization errors for the vertical target components. Note that the errors are small (typically < 2 deg) and quite comparable for the two approximation methods.

E. Saccade dynamics

Figure 12a shows the vectorial velocity profiles for all saccades of the continuous data set from the nonlinear simulator. Most velocity profiles were single-peaked, with some exceptions for very large eye movements that were generated from eccentric initial eye orientations. These velocity profiles, reaching peak velocities near 500 deg/s, qualitatively resemble those seen in human data (e.g., [29], [62]; see Section IX).

Figure 12b quantifies the *main-sequence* property of saccade amplitude, A , vs. $V_{PK} \cdot D$, for the continuous saccade set (cf. Fig. 2e), showing a strong linear relationship, and expressing the fact that most velocity profiles were indeed single-peaked.

Because of the affine dependence of saccade duration on amplitude (Fig. 2c), the peak velocity is expected to saturate for large saccade amplitudes, which is shown in Fig. 12c, where the solid red line is the predicted relation based on the regression in panel b and the $A - D$ relationship. It is described by

$$V_{PK}(A) = \frac{c + d \cdot A}{a + b \cdot A} = \frac{-0.47 + 1.58 \cdot A}{0.048 + 0.0031 \cdot A} \text{ deg/s}$$

which asymptotes at $1.58/0.0031 \approx 510$ deg/s.

We also compared the saccade dynamics of the two approximation methods by comparing the peak velocities of their respective trajectories. Figure 12d shows that the peak velocities were strongly correlated ($r^2=0.993$), and highly similar

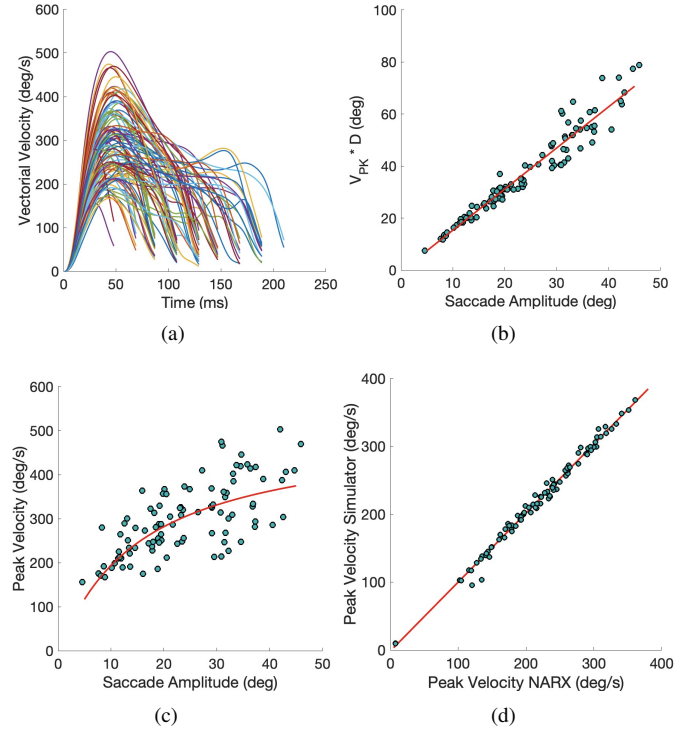


Fig. 12. Dynamics. (a) Vectorial velocity profiles of the continuous saccade set. (b) Amplitude, A vs. $V_{PK} \cdot D$ (in deg). Note the very tight linear relationship ($r^2=0.94$), with an offset of $c=-0.47$ deg and a slope of $d=1.58$. (c) The $A - V_{PK}$ relation saturates for large saccades. The red line follows from the affine $A - D$ relation (with an offset at $a=0.048$ s and a slope $b=0.0031$ s/deg; $r^2: 0.72$; not shown) and the regression in panel (b). All data in (a-c) are from the continuous set generated by the nonlinear simulator. (d) Peak eye velocity for the NARX model vs. the nonlinear simulator (zero-initial set) indicates that both approximations yielded similar dynamics: offset: $= -1.7$ deg/s, slope: 1.02, $r^2: 0.99$.

(slope of the regression line: 1.016). Note that the *main-sequence* relation of the system (Fig. 12c) shows considerable variability in the peak velocity for a given amplitude. Part of this variability, which is also observed in human oblique saccades [29], is due to the strong-direction dependence of the saccade dynamics, and the variation in initial conditions, as these invoke different muscle synergies that significantly influence movement speed. How these synergies are formed is described next.

F. Analysing Muscle Forces

Figure 13 shows the changes in the instantaneous motor control angles of the six tendons for four saccades starting from the center. Several interesting observations can be made. First, pure horizontal saccades (Fig. 13a,b) only involve activation of the tendons m_{MR} and m_{LR} , while vertical saccades require joint action of the vertical recti and obliques (Fig. 13c). For oblique saccades (Fig. 13d), all six tendons are activated. Second, motors act in antagonistic pairs for all saccades, since the main activation controls of the involved muscles are in opposite directions [16], [48], [63]. Third, control of the eye tendons can be characterized as a *pulse-step* activation for the agonists, and an anti-pulse/negative step for the antagonists [21]. Fourth, the positive and negative pulses

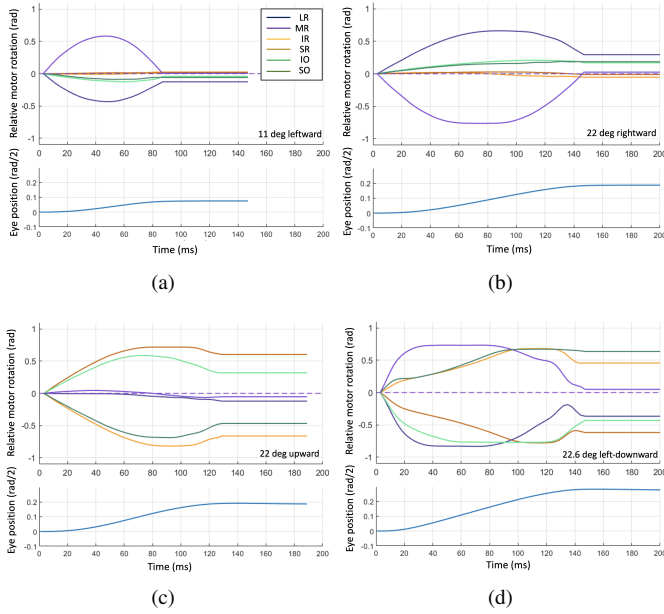


Fig. 13. Changes in motor-command angles (in rad) re. pre-tension for the optimal trajectory of (a) an 11 deg left- and (b) a 22 deg rightward saccade, (c) a 22 deg upward, and (d) a left-downward oblique saccade to [22.6, 22.6] deg, all from straight-ahead. Note that motors form antagonistic muscle pairs with pulse-step/anti-pulse-step behaviors. Note also the different control dynamics for horizontal vs. vertical/torsional systems and the upward action of IO in the vertical saccade. The six muscles contribute to the oblique saccade. Real pre-tension values were [2.01, 1.96, 1.98, 2.03, 1.97, 2.02] rad. Lower panels: vectorial eye position (rad/2).

of the activated agonists and antagonists exactly match the saccade durations, whereas the agonist and antagonist post-saccade steps attain increased and decreased values relative to the initial pre-tensions, respectively. Finally, the pulse (and anti-pulse) amplitudes increase with saccade amplitude. Thus, the net force on the right eye for a rightward horizontal saccade is delivered by the m_{LR} , together with an equally rapid relaxation of the m_{MR} , while the other four tendons stay close to their equilibrium pre-tension values; the slight change in the obliques' tension during larger horizontal saccades is systematic (but note that their net effect is zero). Similarly, an upward saccade requires joint activation of the m_{SR} , m_{IO} muscles and a simultaneous inactivation of the m_{IR} , m_{SO} muscles, and vice versa for a downward saccade, without change in net tension for the horizontal recti (Fig. 13c). Note that all these properties emerged from the optimal control strategy. Interestingly, all have been observed in neurophysiological recordings from monkey oculomotor neurons [16], [18], [48], [63], [46], [47].

TABLE IV
CORRELATIONS: MUSCLE COMMANDS AND VELOCITY COMPONENTS.

	Antagonists			Agonists		Saccade
	LR-MR	SR-IR	SO-IO	SR-IO	SO-IR	$\omega_H - \omega_V$
μ	-0.88	-0.89	-0.49	+0.73	+0.73	0.80
σ	0.12	0.22	0.42	0.24	0.33	0.29
mode	-0.95	-0.99	-0.95	+0.91	+0.94	0.96

Table IV summarizes the correlation statistics between the five different muscle pairs, grouped as antagonists and

agonists, respectively (e.g., Fig. 13d), for all oblique saccade trajectories in the continuous paradigm with a direction at least 20 degrees away from pure horizontal or vertical ($N=57$ saccades). Note that the antagonists have their correlation modes close to -1.0, and the agonists close to +1.0. Note also that the SO-IO muscle pair (antagonists for cyclo-torsion) is more variable than the other four pairs, which is due to Listing's Law that strongly restricts the torsional range in the saccades. The rightmost column shows the correlation statistics of the horizontal and vertical velocity profiles of these oblique saccades. The mode near 1.0 indicates that most trajectories were virtually straight.

IX. DISCUSSION

1) *Summary:* We developed a physics-based model for a biomimetic robotic eye with six independent motors controlling elastic strings, mimicking human eye movement (Fig. 1) by rotating the eye around its fixed center with three degrees of freedom (Fig. 8). The nonlinear system dynamics were learned using a recurrent neural network under optimal control. Our study shows that the control system efficiently produces human-like 3D eye rotations with appropriate saccade characteristics (Figs. 2, 9, 11, 12, 13). Further details on these properties are discussed below.

2) *Nonlinear approximations and pre-tension:* Pre-tension in tendons corresponds to a low static cocontraction of eye muscles in the primate oculomotor system[16], [21]. Despite low reported cocontraction, all eye-muscle neuronal pools exhibit a net neural activity for all static eye positions[18], [21], [48], [46]. This net activity, though not subjected to unexpected loads or gravity, may facilitate fine control of eye orientation by modulating firing rates and overcoming static friction[21]. The push-pull organization with static pre-tension thus enhances angular resolution. In the nonlinear NARX model, only pre-tensions for the central equilibrium orientation were set, ensuring a convex total cost function through trial and error (Fig. 7b). The model is flexible for future complexities and can be applied to directly control a physical robotic eye without explicit mathematical approximations of its physics.

3) *Straight trajectories:* Eye-movement trajectories in the yz plane were straight, despite distinct dynamics for horizontal and vertical saccade components (Fig. 9) and independent control of the six motors. Straight saccades indicate highly correlated velocity profiles, with one component influencing the other[29]. As a consequence, the control signals for the six motors are strongly coupled, dependent on initial eye orientation and target coordinates. The optimal control, emphasizing minimum time to reach the goal (J_D), leads to single-axis rotations by organizing the six motors into a central 3D vectorial eye-velocity generator.

A subset of saccades with higher curvature and lower synchrony likely results from system nonlinearities at large eccentricities and a trade-off in the optimal control objective. Although curvature wasn't explicitly considered in our optimization, movement duration and accuracy cannot both be optimally satisfied simultaneously. Interestingly, similar curvature is observed in saccadic eye movements in humans

and monkeys[62], [60]. Our study offers a quantitative and mechanistic explanation for this observed property.

4) *Nonlinear main-sequence dynamics*: The main-sequence behavior of human saccades is replicated in our biomimetic system (Fig. 12). These non-linear dynamics primarily arise from optimal control implementing a speed-accuracy trade-off, rather than from plant non-linearities[15], [45], [12]. That saccade duration increases with amplitude is already evident in matching pulse/anti-pulse durations of antagonistic motors (Fig. 13). Observations indicate that saccade velocity profiles are positively skewed, with skewness increasing with amplitude[64]. Our simulations also reflect this property to some extent (Fig. 12a), as single-peaked velocity profiles reach their peak at approximately the same time for all amplitudes (for zero-initial saccades: mean 50 ms, std 14 ms). Skewness in our data (time-to- V_{pk} divided by saccade duration) negatively correlates with amplitude ($r=-0.4$).

5) *3D kinematics*: Also Listing's law emerged from the applied optimal control. Although the accuracy cost restricted torsion of the final goal orientation to zero, the optimal control resulted in a tilted plane for the full trajectories in the laboratory frame (Fig. 9a). A minor 18-degree leftward rotation around the z -axis aligned the data with Listing's frame. The slight asymmetry in our robotic eye's muscular geometry, such as $l_{MR} < l_{LR}$, was incompatible with Listing coordinates at zero torsion. This asymmetry was also evident in the xy projection of the training data (Fig. 8). Our previous work[15] demonstrated that Listing's law could automatically emerge by including total fixation force as a fourth cost, systematically tilting the plane in the xz plane after displacing vertical/torsional muscles along the y -axis. We propose that the orientation of Listing's plane and primary position direction result from the specific geometrical arrangement of muscle insertions on the eye and head, combined with their relative lengths and elastic properties.

6) *Antagonistic organisation*: The joint antagonistic activation patterns of the six muscles (Fig. 13) emerged from the optimal control strategy in our model. A horizontal rightward saccade involves a fast contraction (pulse) of the LR muscle and synchronous relaxation (antipulse) of the MR muscle, generating the movement with minimal extra co-contraction (Fig. 13a). Similarly, a purely vertical upward saccade arises from rapid synchronous contraction of SR/IO agonists and relaxation of IR/SO antagonists, maintaining equilibrium pre-tension in horizontal muscles (Fig. 13b). Oblique saccades exhibit complex antagonistic interactions between all six tendons (Fig. 13c).

These emerging synergies align with the pulling directions of each muscle[16], embodying the known "push-pull" organization of the oculomotor and vestibular systems, and reflecting Sherrington's principle of reciprocal innervation[65]. The pulse-step innervations of antagonistic muscle pairs closely resemble their neurobiological counterparts of primate oculomotor neurons[16], [18], [48], [63], [46], [47], reflecting the biomimetic eye's built-in property as an overdamped (nonlinear) filter due to velocity-dependent dynamic friction[66].

7) *Limitations and further study*: Physics-based simulations are important in advancing our understanding of how

movement is controlled. They allow fast and easy exploration of different types of control and system characteristics. However, some aspects can only be realized with real robotic implementations. For this purpose, we have designed and built a robotic spherical eye actuated by six motor driven cables with realistic pulling directions to mimic the six extraocular muscles [67]. Despite the challenges in performing large-scale experiments, the current prototype exhibits the ability to perform a wide range of eye movements with the appropriate characteristics and will be used in future work to validate the computer simulations. Furthermore, by building mechanical prototypes we can realize what the key characteristics are to include in computer simulations. The simulator (Fig. 4) produced realistic human-like saccades and neural control signals but involved simplified approximations compared to the actual robotic system (Fig. 4). Improvements can be made by incorporating more neurobiological and physical realism. First, the tendons are attached to a fixed point on the globe and their paths may pass through the peripheral rim of the eye. More realistically, tendons should wrap around the globe, adjusting their paths as a function of 3D eye orientation. In the primate eye, muscle trajectories are partially fixed to the sclera[50], influencing effective pulling directions that may be further modified by pulleys. Additionally, eye muscles consist of multiple fibers, not a single tendon (Fig. 1), which may further affect iso-innervation trajectories and 3D plant characteristics[16], [48].

Second, our simulations lacked additive and multiplicative noise in control, impacting velocity profile shapes (skewness) and potentially removing the need for an energy cost[12], [45], [68]. Including multiplicative noise may also better align error patterns (Fig. 11a) with human behavior, where errors increase linearly with saccade amplitude.

Finally, we imposed a 3D constraint on movement accuracy that explicitly incorporated Listing's law and the primary position. In our previous work[15], a 2D accuracy cost and a minimized total fixation force sufficed to show how Listing's law related to muscular geometry. With six independent motors, specifying pre-tension was necessary. Designing a quadratic fixation cost, combined with the previous two points, may allow the optimal control to generate Listing's law, the primary position, and specify optimal muscle pre-tension at each eye orientation—an area for future exploration.

X. CONCLUSION

This paper has demonstrated how model-based optimal control principles can explain stereotyped human oculomotor behaviors, through simulations in a realistic model of the human eye with a cable-driven actuation system that mimics the six degrees of freedom of the extraocular muscles. Previous work has addressed only systems with 1-3 degrees of freedom. This article is the first study of a six-muscle system design, which introduced novel challenges. We proposed nonlinear optimal control techniques to optimize the accuracy, energy, and duration of eye movement trajectories, and we used a recurrent neural network that learned to emulate the nonlinear system dynamics from the recorded sample trajectories. We

showed that realistic three-dimensional rotational kinematics and dynamics, as seen in human saccades, emerged from our model and that the six cables organized themselves into appropriate antagonistic muscle pairs, as in the primate oculomotor system. This research has demonstrated the potential of robotic models to test theories on the behavior of humans or animals, and to help understand many aspects of intelligence and control in natural systems.

ACKNOWLEDGMENT

This research was supported by the European Union's Horizon 2020 program, ERC Advanced Grant, 2016 (project ORIENT, grant nr. 693400); the Donders Centre for Neuroscience, Radboud University (AJVO); the HAVATAR project (DOI: 10.54499/PTDC/EEI-ROB/1155/2020); LARSyS funding (DOI: 10.54499/LA/P/0083/2020, 10.54499/UIDP/50009/2020 and 10.54499/UIDB/50009/2020).

REFERENCES

- [1] D. Lambrinos, H. Kobayashi, R. Pfeifer, M. Maris, T. Labhart, and R. Wehner, "An autonomous agent navigating with a polarized light compass," *Adaptive Behav.*, vol. 6, pp. 131–161, 1997.
- [2] B. Webb, "Can robots make good models of biological behaviour?" *Behav. Brain Sci.*, vol. 24, p. 1033–1050, 2001.
- [3] J. Lee, S. N. Sponberg, O. Y. Loh, A. G. Lamperski, R. J. Full, and N. J. Cowan, "Templates and anchors for antenna-based wall following in cockroaches and robots," *IEEE Trans. Robotics*, vol. 24, pp. 130–143, 2008.
- [4] S. Sponberg and R. J. Full, "Neuromechanical response of musculoskeletal structures in cockroaches during rapid running on rough terrain," *J. Exp. Biol.*, vol. 211, pp. 433–446, 02 2008.
- [5] J. Stankiewicz and B. Webb, "Looking down: a model for visual route following in honey bees," *Bioinspir. Biomim.*, 2021.
- [6] Z. Lyu and Q. Xu, "Design of a new bio-inspired dual-axis compliant micromanipulator with millimeter strokes," *IEEE Trans. Robotics*, pp. 1–15, 2022.
- [7] G. Cannata and M. Maggiali, "Models for the design of bioinspired robot eyes," *IEEE Trans. Robotics*, vol. 24, pp. 27–44, 2008.
- [8] E. Maini, G. Teti, M. Rubino, C. Laschi, and P. Dario, "Bio-inspired control of eye-head coordination in a robotic anthropomorphic head," in *BioRob*, 2006, pp. 549–554.
- [9] M. Argyle, R. Ingham, F. Alkema, and M. McCallin, *The different functions of gaze*. Walter de Gruyter, Berlin/New York Berlin, New York, 1973.
- [10] T. V. Wouwe, L. H. Ting, and F. D. Groote, "An approximate stochastic optimal control framework to simulate nonlinear neuro-musculoskeletal models in the presence of noise," *PLOS Computational Biology*, vol. 18, no. 6, p. e1009338, 2022.
- [11] A. Bersani, G. Davico, and M. Viceconti, "Modeling human suboptimal control: A review," *Journal of Applied Biomechanics*, vol. 39, no. 5, pp. 294–303, 2023.
- [12] C. M. Harris and D. M. Wolpert, "The main sequence of saccades optimizes speed-accuracy trade-off," *Biol. Cybernet.*, vol. 95, pp. 21–29, 2006.
- [13] R. J. van Beers, "Saccadic eye movements minimize the consequences of motor noise," *PLOS One*, vol. 3, pp. 1–8, 04 2008.
- [14] S. Saeb, C. Weber, and J. Triesch, "Learning the optimal control of coordinated eye and head movements," *PLOS Comp. Biol.*, vol. 7, p. e1002253, 2011.
- [15] A. John, C. Aleluia, A. J. Van Opstal, and A. Bernardino, "Modelling 3d saccade generation by feedforward optimal control," *PLOS Comp. Biol.*, vol. 17, pp. 1–35, 05 2021.
- [16] D. A. Robinson, "A quantitative analysis of extraocular muscle cooperation and squint," *Investig. Ophthalmol.*, vol. 14, pp. 801–825, 1975.
- [17] R. S. Snell and M. A. Lemp, *Clinical anatomy of the eye*. John Wiley & Sons, 2013.
- [18] D. A. Robinson and E. L. Keller, "The behavior of eye movement motoneurons in the alert monkey," *Bibl Ophthalmol.*, vol. 82, pp. 7–16, 1972.
- [19] S. N. Kosari, S. Ramadurai, H. J. Chizeck, and B. Hannaford, "Control and tension estimation of a cable driven mechanism under different tensions," in *Proc. ASME Int. Design Eng. Tech. Conf.*, vol. V06AT07A077. ASME, 2013.
- [20] M. Haghighipناه, M. Miyasaka, and B. Hannaford, "Utilizing elasticity of cable-driven surgical robot to estimate cable tension and external force," *IEEE RA-L*, vol. 2, pp. 1593–1600, 2017.
- [21] D. A. Robinson, "Modeling the oculomotor control system," *Prog. Brain Res.*, vol. 267, pp. 1–435, 2022.
- [22] F. C. Donders, *The 11th yearly report of the Netherlands Hospital for Necessitous Eye Patients (in Dutch)*. Van de Weijer, Utrecht, The Netherlands, 1870, vol. 11.
- [23] D. Tweed and T. Vilis, "Implications of rotational kinematics for the oculomotor system in three dimensions," *J. Neurophysiol.*, vol. 58, pp. 832–849, 1987.
- [24] K. Hepp, "On listings law," *Commun. Math. Phys.*, vol. 132, pp. 285–292, 1990.
- [25] A. J. Van Opstal, K. Hepp, B. J. M. Hess, D. Straumann, and V. Henn, "Two-, rather than three-dimensional representation of saccades in monkey superior colliculus," *Science*, vol. 252, pp. 1313–1315, 1991.
- [26] T. Haslwanter, "Mathematics of three-dimensional eye rotations," *Vision Res.*, vol. 35, pp. 1727–1739, 1995.
- [27] D. Tweed, B. Glenn, and T. Vilis, "Eye-head coordination during large gaze shifts," *J. Neurophysiol.*, vol. 73, pp. 766–779, 1995.
- [28] A. T. Bahill, M. R. Clark, and L. Stark, "The main sequence: a tool for studying human eye movements," *Math. Biosci.*, vol. 24, pp. 191–204, 1975.
- [29] J. A. M. Van Gisbergen, A. J. Van Opstal, and J. J. M. Schoenmakers, "Experimental test of two models for the generation of oblique saccades," *Exp. Brain Res.*, vol. 57, pp. 321–336, 1985.
- [30] S. K. Rajendran, Q. Wei, N. Yao, and F. Zhang, "Design, implementation, and observer-based output control of a super-coiled polymer-driven two degree-of-freedom robotic eye," *IEEE Robotics and Automation Letters*, vol. 8, no. 9, pp. 5958–5965, 2023.
- [31] X. yin Wang, Y. Zhang, X. jie Fu, and G. shan Xiang, "Design and kinematic analysis of a novel humanoid robot eye using pneumatic artificial muscles," *J. Bionic Eng.*, vol. 5, pp. 264–270, 2008.
- [32] M. Lakzadeh, "A biologically-inspired eye model for testing oculomotor control theories," Master's thesis, University of British Columbia, 2012. [Online]. Available: <https://open.library.ubc.ca/collections/ubctheses/24/items/1.0072549>
- [33] Q. Wei, S. Sueda, and D. K. Pai, "Physically-based modeling and simulation of extraocular muscles," *Prog. Biophys. Mol. Biol.*, vol. 103, pp. 273–283, 2010, special Issue on Biomechanical Modelling of Soft Tissue Motion.
- [34] A. Priamnikov, M. Fronius, B. Shi, and J. Triesch, "OpenEyeSim: A biomechanical model for simulation of closed-loop visual perception," *J. Vision*, vol. 16, pp. 25–25, 12 2016.
- [35] J. Iskander, M. Hossny, S. Nahavandi, and L. del Porto, "An ocular biomechanical model for dynamic simulation of different eye movements," *J. Biomech.*, vol. 71, pp. 208–216, 2018.
- [36] S. Schulz, S. M. z. Borgsen, and S. Wachsmuth, "See and be seen – rapid and likeable high-definition camera-eye for anthropomorphic robots," in *ICRA* 2019, 2019, pp. 2524–2530.
- [37] H. Liu, J. Luo, P. Wu, S. Xie, and H. li, "Symmetric kullback-leibler metric based tracking behaviors for bioinspired robotic eyes," *Appl. Bionics Biomech.*, vol. 2015, pp. 1–11, 11 2015.
- [38] D. Dansereau, D. Wood, S. Montabone, and S. B. Williams, "Exploiting parallax in panoramic capture to construct light fields," in *ICRA* 2014, 2014.
- [39] N. F. Duarte, M. Rakovic, J. Tasevski, M. I. Coco, A. Billard, and J. Santos-Victor, "Action anticipation: Reading the intentions of humans and robots," *IEEE RA-L*, vol. 3, pp. 4132–4139, 2018.
- [40] T. Kanda, H. Ishiguro, T. Ono, M. Imai, and R. Nakatsu, "Development and evaluation of an interactive humanoid robot" robovie", in *ICRA* 2002, vol. 2. IEEE, 2002, pp. 1848–1855.
- [41] Y. Mohammad, S. Okada, and T. Nishida, "Autonomous development of gaze control for natural human-robot interaction," in *Proc. 2010 workshop Eye Gaze Intell. Human-Mach. Interaction*, 2010, pp. 63–70.
- [42] E. S. Maini, L. Manfredi, C. Laschi, and P. Dario, "Bioinspired velocity control of fast gaze shifts on a robotic anthropomorphic head," *Auton. Robots*, vol. 25, pp. 37–58, 2008.
- [43] S. K. Rajendran, Q. Wei, and F. Zhang, "Two degree-of-freedom robotic eye: Design, modeling, and learning-based control in foveation and smooth pursuit," *Bioinspir. Biomim.*, vol. 16, 05 2021.

- [44] M. R. C. Lucas, "Construction and Characterization of a Biomimetic Robotic Eye Model with Three Degrees of Rotational Freedom: A Testbed for Neural Control of Eye Movements," Master's thesis, University of Lisbon, 2017.
- [45] R. Shadmehr and S. Mussa-Ivaldi, *Biological learning and control: how the brain builds representations, predicts events, and makes decisions* (Chapter 11). MIT Press, 2012.
- [46] A. F. Fuchs and E. S. Luschei, "Firing patterns of abducens neurons of alert monkeys in relationship to horizontal eye movement," *J. Neurophysiol.*, vol. 33, pp. 383–392, 1970.
- [47] —, "The activity of single trochlear nerve fibers during eye movements in the alert monkey," *Exp Brain Res*, vol. 13, pp. 78–89, 1971.
- [48] K. Hepp and V. Henn, "Iso-frequency curves of oculomotor neurons in the rhesus monkey," *Vision Res*, vol. 25, pp. 493–499, 1985.
- [49] J. L. Demer, "Current concepts of mechanical and neural factors in ocular motility," *Curr. Opinion Neurol.*, vol. 19, pp. 4–13, 2006.
- [50] K.-M. Lee, A. P. Lai, J. Brodale, and A. Jampolsky, "Sideslip of the medial rectus muscle during vertical eye rotation," *Investig. Ophthalm. Vis. Sci.*, vol. 48, pp. 4527–4533, 2007.
- [51] B. Dias, "Modeling, simulation, analytic linearization and optimal control of a 6 tendon-driven biomimetic eye: a tool for studying human oculomotor control," Master thesis, 2021. [Online]. Available: <https://fenix.tecnico.ulisboa.pt/cursos/meec/dissertacao/846778572212806>
- [52] J. M. Miller and D. A. Robinson, "A model of the mechanics of binocular alignment," *Comp. Biomed. Res.*, vol. 17, pp. 436–470, 1984.
- [53] J. Rychlewski, "On hooke's law," *J. Appl. Math Mech.*, vol. 48, pp. 303–314, 1984.
- [54] G. Wu and K. Sreenath, "Variation-based linearization of nonlinear systems evolving on $so(3)$ and s^2 ," *IEEE Access*, vol. 3, pp. 1592–1604, 2015.
- [55] T. Lin, B. Horne, P. Tino, and C. Giles, "Learning long-term dependencies in narx recurrent neural networks," *IEEE Transactions on Neural Networks*, vol. 7, no. 6, pp. 1329–1338, 1996.
- [56] H. Siegelmann, B. Horne, and C. Giles, "Computational capabilities of recurrent narx neural networks," *IEEE Transactions on Systems, Man, and Cybernetics, Part B (Cybernetics)*, vol. 27, no. 2, pp. 208–215, 1997.
- [57] T. G. Thuruthel, E. Falotico, F. Renda, and C. Laschi, "Learning dynamic models for open loop predictive control of soft robotic manipulators," *Bioinspir. Biomim.*, vol. 12, p. 066003, 2017.
- [58] R. Shadmehr, J. J. O. De Xivry, M. Xu-Wilson, and T.-Y. Shih, "Temporal discounting of reward and the cost of time in motor control," *J. Neurosci.*, vol. 30, pp. 10 507–10 516, 2010.
- [59] L. Ljung, *System Identification (2nd Ed.): Theory for the User*. USA: Prentice Hall PTR, 1999.
- [60] A. C. Smit and J. A. M. Van Gisbergen, "An analysis of curvature in fast and slow human saccades," *Experimental Brain Research*, vol. 81, pp. 335–345, 1990.
- [61] A. J. Van Opstal and J. A. M. Van Gisbergen, "Scatter in the metrics of saccades and properties of the collicular motor map," *Vision Res*, vol. 29, pp. 1183–1196, 1989.
- [62] A. C. Smit, A. J. Van Opstal, and J. A. M. Van Gisbergen, "Component stretching in fast and slow oblique saccades in the human," *Experimental Brain Research*, vol. 81, pp. 325–334, 1990.
- [63] Y. Suzuki, D. Straumann, J. I. Simpson, K. Hepp, and V. Henn, "Three-dimensional extra-ocular motoneuron innervation in the rhesus monkey. i: Muscle rotation axes and the on-directions during fixation," *Exp Brain Res*, vol. 126, pp. 187–199, 1999.
- [64] A. J. Van Opstal and J. A. M. Van Gisbergen, "Skewness of saccadic velocity profiles: a unifying parameter for normal and slow saccades," *Vision Res*, vol. 27, pp. 731–745, 1987.
- [65] C. S. Sherrington, *The Integrative Action of the Nervous System*. Oxford University Press, 1906.
- [66] D. A. Robinson, "The mechanics of human saccadic eye movement," *J. Physiol.*, vol. 174, pp. 245–264, 1964.
- [67] A. John, J. van Opstal, and A. Bernardino, "A cable-driven robotic eye for understanding eye-movement control," in *2023 9th International Conference on Automation, Robotics and Applications (ICARA)*, 2023, pp. 128–133.
- [68] R. Cardoso, "Feedback control on a model of a 3d biomimetic robotic eye," Master thesis, 2019. [Online]. Available: https://fenix.tecnico.ulisboa.pt/downloadFile/1689244997260701/thesis_finalissima.pdf



Reza Javanmard Alitappeh (PhD 2016) is an Assistant Professor at the University of Science and Technology of Mazandaran, Iran. He joined the ORIENT project, Instituto Superior Tecnico (IST), ISR, Lisbon. In 2019 he worked as a research fellow at Visual Artificial Intelligence Laboratory in Oxford Brookes University (UK) on autonomous vehicles. He completed his PhD in AI & robotics at UFMG, Brazil. His research interests are robotics, machine learning, and machine vision.



Akhil John (MSc. 2018) is a PhD candidate at the Department of Electrical and Computer Engineering and a member of the VisLab at IST, Lisbon, Portugal. He graduated from BITS Pilani, India, with a bachelor's degree in mechanical engineering and a master's degree in physics. His research interests include mechanical design, control theory, computer vision, and neuroscience. His PhD research aims to study eye saccade control using a cable-driven robotic platform and use it for robotic vision.



Bernardo Dias (M.Sc. 2020) is a graduate student from Electrical and Computer Engineering at IST, Lisbon. He was a research fellow at the Institute for Systems and Robotics at IST for two years where he developed his master thesis and research on modeling and controlling a 6 DoF biomimetic eye, designed according to the kinematics of the human eye.



A. John van Opstal (PhD 1989) is a professor of biophysics at the Donders Center for Neuroscience at Radboud University Nijmegen. He studies and models neural sound-localization mechanisms, multisensory integration, and the neurophysiology of saccadic eye-head gaze shifts. He published more than 130 articles (GScholar: h-index 53) and "The Auditory System and Human Sound-Localization Behavior" (Elsevier, 2016). He graduated 30 Ph.D. students and received an ERC advanced grant in 2016.



Alexandre Bernardino (PhD 2004) is a tenured Associate Professor and Senior Researcher at the Institute for Systems and Robotics at IST, Lisbon University. He published more than 300 research papers and participated in more than 20 national and international research projects, being the principal investigator in 5 of them. His main research interests focus on the application of computer vision, machine learning, cognitive science, and control theory to advanced robotics and automation systems.